Nanoscale

ROYAL SOCIETY OF CHEMISTRY

PAPER

View Article Online
View Journal | View Issue

Cite this: *Nanoscale*, 2024, **16**, 14310

Embedding AIE-type $Ag_{28}Au_1$ nanoclusters within ZIF-8 for improved photodynamic wound healing through bacterial eradication†

Qiuxia He,[a] Zhen Jiang,[a] Hongli Jiang,[c] Songjie Han,[a] Guoping Yang, *[b] Xun Yuan *[a] and Haiguang Zhu *[a]

Designing antibacterial agents with rapid bacterial eradication performance is paramount for the treatment of bacteria-infected wounds. Metal nanoclusters (NCs) with aggregation-induced emission (AIE) have been considered as novel photodynamic antibacterial agents without drug resistance, but they suffer from poor photostability and low charge carrier separation efficiency. Herein, we report the design of a photodynamic antibacterial agent by encapsulating AIE-type AgAu NCs ($Ag_{28}Au_1$ NCs) into a zeolitic Zn(2-methylimidazole)$_2$ framework (ZIF-8). The encapsulation of AIE-type $Ag_{28}Au_1$ NCs into porous ZIF-8 could not only enhance the photostability of $Ag_{28}Au_1$ NCs by inhibiting their aggregation but also promote the separation of photoinduced charge carriers, resulting in the rapid generation of destructive reactive oxygen species (ROS) for bacterial killing under visible-light irradiation. Consequently, the as-designed photodynamic $Ag_{28}Au_1$ NCs@ZIF-8 antibacterial agent could rapidly eliminate 97.7% of *Escherichia coli* (*E. coli*) and 91.6% of *Staphylococcus aureus* (*S. aureus*) within 5 min *in vitro* under visible light irradiation. Furthermore, *in vivo* experimental results have highlighted the synergistic effect created by AIE-type $Ag_{28}Au_1$ NCs and ZIF-8, enabling $Ag_{28}Au_1$ NCs@ZIF-8 to effectively eradicate bacteria in infected areas, reduce inflammation, and promote the generation of blood vessels, epithelial tissue, and collagen. This synergistic effect promoted the healing of *S. aureus*-infected wound, with nearly 100% of wound recovery within 11 days. This work may be interesting because it sheds light on the design of metal NC-based photodynamic nanomedicine for bacteria-infected disease treatment.

Received 23rd April 2024,
Accepted 20th June 2024

DOI: 10.1039/d4nr01769b

rsc.li/nanoscale

1. Introduction

Wound infections, afflicting over several million people each year, are a growing public health threat.[1–5] Open wounds provide a rapid breeding ground for pathogenic bacteria, such as *Escherichia coli* (*E. coli*) and *Staphylococcus aureus* (*S. aureus*), thus impeding wound healing and increasing the risk of severe infection-related syndromes such as localized septic infection, sepsis, acute renal failure, and even death.[6–8] Therefore, rapid bacterial eradication in infected areas is crucial for effective treatment. While antibiotic therapy is a common clinical strategy,[9,10] the low antibacterial efficiency of antibiotics could cause the formation of biofilms, leading to a high failure rate of treatment.[11] Furthermore, antibiotic abuse can accelerate bacterial resistance, resulting in the emergence of superbacteria.[12] Hence, there is an urgent need to develop a fast antimicrobial strategy for wound infection treatment.

Recently, antimicrobial photodynamic therapy has emerged as a promising strategy for treating bacteria-infected wounds.[13–15] This therapy harnesses reactive oxygen species (ROS) generated from photocatalysts under light irradiation to rapidly kill bacteria without inducing antimicrobial resistance.[13,16] Consequently, extensive research has been conducted to develop efficient photocatalysts for wound infection treatment.[17] Metal nanoclusters (NCs) with aggregation-induced emission (AIE), such as gold NCs (Au NCs),[18–22] silver NCs (Ag NCs),[23–25] or alloy NCs (AuAg NCs),[26–28] are considered as good candidates due to their photochemical properties (*e.g.*, a large Stokes shift, a high content of metal(I) components, strong photoluminescence (PL),[29–31] and a long-lived PL lifetime[32–34]). Metal NC-based antibacterial agents traditionally function by sacrificing themselves, either through

[a]*College of Materials Science and Engineering, Qingdao University of Science and Technology (QUST), 53 Zhengzhou Rd., Shibei District, Qingdao 266042, P. R. China. E-mail: yuanxun@qust.edu.cn, zhuhg@qust.edu.cn*
[b]*School of Chemistry, Biology and Material Science, Jiangxi Province Key Laboratory of Synthetic Chemistry, Jiangxi Key Laboratory for Mass Spectrometry and Instrumentation, East China University of Technology, Nanchang 330013, China*
[c]*Department of Respiratory and Critical Care Medicine, Qingdao Eighth People's Hospital, Qingdao 266121, China*
† Electronic supplementary information (ESI) available. See DOI: https://doi.org/10.1039/d4nr01769b

metal ion release or cell adhesion/internalization, in order to kill bacteria. This self-consumed antibacterial action, however, renders them ineffective for long-lasting bacterial killing. In contrast, AIE-type metal NCs have the unique ability to generate ROS under light illumination, which effectively deactivates bacteria. This characteristic offers an innovative approach to achieving reliable and durable photodynamic bacterial inactivation, serving as an alternative to traditional methods based on advanced oxidation techniques.[35] However, the ultrasmall size of AIE-type metal NCs usually leads to structural decomposition and fast recombination of the photogenerated carriers, hindering their utility in photodynamic therapy.[36] To address this limitation, encapsulating metal NCs into a rigid porous material to strengthen stability and promote separation of photogenerated carriers might be a feasible strategy.[37] In this regard, metal–organic frameworks (MOFs) are good porous candidates. MOFs, with their highly ordered structures and ultrahigh porosity, provide a platform to immobilize metal NCs.[21] Additionally, most MOFs are semiconductors with a large energy-band gap, enabling them to serve as electron acceptors to promote the separation of photogenerated charge carriers for other photocatalysts.[38] MOFs can also promote wound healing by facilitating cell proliferation or differentiation.[39,40] Therefore, we hypothesize that if we could encapsulate metal NCs into the porous structure of MOFs, we may overcome the challenges of poor photostability and fast recombination of photogenerated carriers in AIE-type metal NCs, thereby achieving rapid and sustained sterilization for wound healing.

Herein, we report the design of a photodynamic antibacterial agent for rapid photodynamic bacterial eradication facilitating wound healing by encapsulating AIE-type bimetallic AgAu NCs (namely, $Ag_{28}Au_1$ NCs, protected by dihydrolipoic acid (DHLA)) into a zeolitic Zn(2-methylimidazole)$_2$ framework (ZIF-8) (Scheme 1). The key design feature is the employment of ZIF-8 as a porous matrix, which serves to enhance the photostability of the $Ag_{28}Au_1$ NCs by preventing their migration and subsequent aggregation. Furthermore, ZIF-8 acts as an electron acceptor, facilitating the efficient separation of photogenerated charge carriers in the $Ag_{28}Au_1$ NCs, thereby ensuring the rapid generation of ROS essential for fast bacterial eradication. This novel design of the photodynamic antibacterial agent (namely, $Ag_{28}Au_1$ NCs@ZIF-8) demonstrated a notable capability for rapid bacterial inactivation under visible light irradiation *in vitro*, along with a favorable wound healing effect *in vivo*. The outcomes of this study highlight the promising photodynamic therapeutic potential of the proposed agent in addressing wound infections, potentially opening up new avenues for future research endeavors on developing other NC-based photodynamic antibacterial agents for the treatment of bacteria-infected wounds.

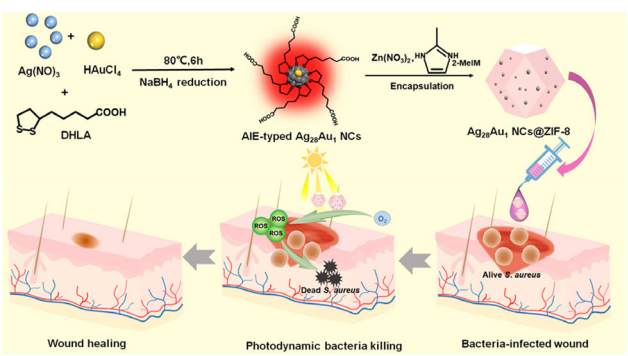

Scheme 1 Schematic diagram of the preparation of $Ag_{28}Au_1$ NCs@ZIF-8 antibacterial agents for enhanced wound healing *via* rapid photodynamic bacterial eradication.

2. Experimental section

2.1. Chemicals and materials

Chloroauric acid ($HAuCl_4$, ≥99.9%), silver nitrate ($AgNO_3$, ≥99.8%), sodium hydroxide (NaOH, ≥96%), ethanol (C_2H_5OH, ≥99.0%), zinc nitrate ($Zn(NO_3)_2{\cdot}6H_2O$, ≥99.0%), 2-methylimidazole (≥99.8%), acetonitrile (CH_3CN, ≥99%), glutaraldehyde solution ($C_5H_8O_2$, 25%–28%), and 2,7-dichlorodihydrofluorescein diacetate (DCFH-DA) dye were purchased from Sinopharm Chemical Reagent Co., Ltd. Alphalipoic acid (DHLA, ≥99%) and sodium tetrahydroborate ($NaBH_4$, ≥96%) were purchased from Shanghai Shanpu Chemical Co., Ltd (China). Formalin solution was purchased from Merck. Ultrapure water was used throughout the experiments. Phosphate buffer solution (PBS), Luria–Bertani (LB) nutrient agar, and LB broth were purchased from Qingdao Hope Bio-Technology Co., Ltd. Carbomer 940 was purchased from Shanghai McLean Biochemical Co., Ltd. A complete Dulbecco's modified Eagle's medium (DMEM) was purchased from Beijing Solarbio Science & Technology Co., Ltd. Standard strains of *Staphyloccocus aureus* ATCC 6538 (*S. aureus*) and *Escherichia coli* ATCC 25922 (*E. coli*) were purchased from China General Microbiological Culture Collection Center.

The animals were purchased from China Weitong Lihua Animal Co., Ltd., and female ICR mice aged 6 weeks were selected. Animals were maintained under specific pathogen-free conditions and fed *ad libitum*. Animal experiments were conducted according to the international ethics guidelines and the National Institutes of Health Guide concerning the Care and Use of Laboratory Animals.

2.2. Instrumentation

The size and morphology of samples were observed using a transmission electron microscope (TEM, JEM-2100 Plus Electron Microscope) and a scanning electron microscope (SEM, JSM-6700F). The elemental mapping results of $Ag_{28}Au_1$ NCs@ZIF-8 were obtained using an energy dispersive spectrometer (EDS, OXFORD MAX-80, INCA SYSTEM). The optical properties of $Ag_{28}Au_1$ nanoclusters (NCs) and the turbidity of bacteria were measured by UV-vis absorption spectroscopy using a Shimadzu UV-1800 spectrometer. The molecular weight of $Ag_{28}Au_1$ NCs was analyzed by electrospray ionization-mass

spectrometry (ESI-MS, Bruker Impact II). Fourier transform infrared (FTIR) spectra of $Ag_{28}Au_1$ NCs@ZIF-8 and ZIF-8 were recorded from 3800 to 450 cm^{-1} using a Horiba-Jobin Yvon FluoroMax-4 fluorescence spectrophotometer. The content of the Zn^{2+} in the hydrogel and that released from the hydrogel was determined by inductively coupled plasma mass spectrometry (ICP-MS, Agilent 720-ES). X-ray photoelectron spectroscopy (XPS) data were obtained using an X-ray photoelectron spectrometer (ESCALAB MK II Axis Ultra Dld system). X-ray diffraction (XRD) patterns were obtained using an X-ray diffractometer (D-Max 2500/PC). The time-resolved photoluminescence (PL) spectrum was recorded using a time-resolved PL spectrometer (FLS-1000).

2.3. Preparation of AIE-type $Ag_{28}Au_1$ NCs

$AgNO_3$ (20 mM) solution and $HAuCl_4$ (20 mM) solution were prepared using water, and DHLA (50 mM) solution was prepared using 3 mL NaOH (71.4 mM) solution. In a typical synthesis of highly luminescent $Ag_{28}Au_1$ NCs, 2.897 mL of $AgNO_3$ (20 mM) and 0.103 mL of $HAuCl_4$ (20 mM) were first added to DHLA (50 mM, 6 mL) solution and stirred for 10 min to synthesize DHLA–metal(I) complexes. Subsequently, a newly prepared $NaBH_4$ (100 mM, 1.2 mL) aqueous solution was added to the reaction system, stirred at room temperature for 6 h, and then heated at 80 °C for 2 h to synthesize a highly luminescent $Ag_{28}Au_1$ NC solution. The obtained $Ag_{28}Au_1$ NCs were purified by centrifuging the mixture ($Ag_{28}Au_1$ NCs : acetonitrile = 1 : 3 volume ratio) at 8000 rpm for 5 min. The obtained solids of Au NCs were redissolved in 10 mL of H_2O for further use.

2.4. Preparation of DHLA-protected Ag_{29} NCs

3 mL of $AgNO_3$ (20 mM) was first added to DHLA (50 mM, 6 mL) solution and stirred for 10 min to synthesize DHLA–metal(I) complexes. Subsequently, the newly prepared $NaBH_4$ (100 mM, 1.2 mL) aqueous solution was added to the reaction system, stirred at room temperature for 6 h, and then heated at 80 °C for 2 h to synthesize a DHLA-protected Ag_{29} NC solution. The obtained NCs were purified by centrifuging the mixture ($Ag_{28}Au_1$ NCs : acetonitrile = 1 : 3 volume ratio) at 8000 rpm for 5 min. The obtained solids of $Ag_{28}Au_1$ NCs were redissolved in 10 mL of H_2O for further use.

2.5. Preparation of $Ag_{28}Au_1$ NCs@ZIF-8

5.4 mL of $Ag_{28}Au_1$ NC solution was introduced into a beaker containing 34.60 mL of water. Subsequently, 162.8 μL of $Zn(NO_3)_2$ (0.49 M) solution was added to the beaker under stirring at room temperature for 1 h, followed by adding 1.62 mL of 2-methylimidazole (3.456 M) under stirring for another 10 min. The reaction was allowed to stay at room temperature for 6 h without stirring. Finally, the red-brown precipitate was collected by centrifugation, washed five times with water, and dried under vacuum at room temperature for 24 h to obtain $Ag_{28}Au_1$ NCs@ZIF-8.

2.6. Preparation of ZIF-8

1.628 mL of $Zn(NO_3)_2$ (0.49 M) solution was added to a beaker containing 16.2 mL of 2-methylimidazole (3.456 M) under stirring for 10 min. The reaction was allowed to stay at room temperature for 6 h without stirring. Finally, the white precipitate was collected by centrifugation, washed five times with water, and dried under vacuum at room temperature for 24 h to obtain ZIF-8.

2.7. Photodynamic antibacterial test

Gram-negative *E. coli* and Gram-positive *S. aureus* were used as bacterial models to evaluate the photodynamic bactericidal activity of the photodynamic antibacterial agents under visible light irradiation. All the glassware and medium solutions were sterilized in an autoclave at 121 °C for 30 min before the antibacterial test. All tests were performed under sterile conditions. Bacterial cells were cultured in LB medium on a shaking table at 37 °C for 18 h, centrifuged at 8000 rpm for 5 min to remove metabolites, and finally diluted with PBS solution (0.01 M, pH 7.4) to obtain a bacterial suspension with a cell count of 10^7 CFU mL^{-1}. In a typical antibacterial experiment, ZIF-8 (4.65 mg), $Ag_{28}Au_1$ NCs (0.35 mg), their blended sample (4.65 mg of $Ag_{28}Au_1$ NCs and 0.35 mg of $Ag_{28}Au_1$ NCs, $Ag_{28}Au_1$ NCs + ZIF-8), and $Ag_{28}Au_1$ NCs@ZIF-8 (5 mg) were separately mixed with 5 mL of bacterial suspension, respectively. Irradiation was performed using a commercial 300 W xenon lamp with an optical cut-off filter (λ = 400–1100 nm, 100 mW cm^{-2}, CEL-HXF300, Beijing China Education AuLight Technology (CEAuLight) Co., Ltd). Then, at the given irradiation interval (0, 5, 10, 15, 20 min), 100 μL of bacterial suspension was coated on a fresh agar plate and cultured at 37 °C for 24 h. Finally, the colonies growing on the plate were counted to determine the number of viable bacteria after culture. In addition, the corresponding control tests were performed under the same conditions (for example, antimicrobial tests with or without the use of antimicrobials under visible light irradiation or dark conditions).

2.8. ROS assay

The intracellular ROS levels were analyzed by using fluorescent 2′,7′-dichlorofluorescein (DCF) dye as the indicator, which was produced through the oxidation of DCFH-DA by ROS. In brief, a mixed solution of 5 mL of *E. coli* and 5 mg of the $Ag_{28}Au_1$ NCs@ZIF-8 antibacterial agent was firstly irradiated with visible light under O_2 bubbling for 20 min. Subsequently, 10 μL of DCFH-DA (200 μM) was introduced into the mixed solution and incubated for 20 min at 37 °C to ensure the oxidation of DCFH-DA by ROS. After that, the bacterial suspension was centrifuged at 5000 rpm for 5 min, washed three times with PBS, and re-suspended in PBS to the original volume (1 mL). The concentration of the resulting DCF was determined by recording its PL intensity on a microplate reader at an excitation/emission wavelength of 488/525 nm. In addition, bacterial suspensions treated with $Ag_{28}Au_1$ NCs and ZIF-8 were subjected to the same conditions.

2.9. Cytotoxicity assessment

The cytotoxicity of various antibacterial agents was evaluated using a cell proliferation kit (MTT) with the HeLa cell as a cell model. Firstly, the cells were seeded in a 96-well plate and cultured under standard culture conditions (37 °C, 5% CO_2) for 24 h. The antibacterial agent (dispersed in carbomer) was put into wells for irradiation or darkness treatment. After post-seeding for 24 h, 20 μL of the MTT solution was added into the wells and allowed to culture in an incubator for 4 h. Afterwards, the MTT solution was discarded, and DMSO was added to the wells. After stationary culture for 30 min, the optical density of the supernatants in the 96-well plate was measured at 570 nm using a microplate reader.

2.10. Animal experiments

All animal experiments were approved by the Biomedical Ethics Committee of Qingdao Zhong Hao Biological Engineering Co., Ltd (Qingdao, China). The mice were randomly assigned to 4 groups, with 3 mice in each group, according to the samples: control (carbomer), ZIF-8 (dispersed in carbomer), $Ag_{28}Au_1$ NCs (dispersed in carbomer), and $Ag_{28}Au_1$ NCs@ZIF-8 (dispersed in carbomer). The mice were anesthetized with isoflurane (2%) and had their back hair removed with a depilatory cream. A skin biopsy perforator (8 mm in diameter) was used to create a full-thickness wound on the pasteurized dorsal skin. The wound sites were inoculated with *S. aureus* suspensions (100 μL, 10^8 CFU mL^{-1}), covered with 3 M films, and left for 1 day to develop severe infection. Subsequently, the infected wounds were treated with various photodynamic antibacterial agents (200 μL, 1 mg mL^{-1}) and carbomer (200 μL, control). Afterwards, the infected wounds were irradiated with a commercial 300 W xenon lamp with an optical cut-off filter (λ > 400 nm, 100 mW cm^{-2}) for 5 min each day. After being treated for eleven days, all mice were sacrificed and the surrounding wound tissues were collected and fixed in paraformaldehyde (4%) for further H&E staining and Masson trichrome staining. Blood was collected and used to detect the levels of IL-6, IL-1β, and TNF-α.

3. Results and discussion

3.1. Synthesis and characterization of $Ag_{28}Au_1$ NCs@ZIF-8

In this study, highly luminescent AuAg alloy NCs with AIE were chosen as the NC model. The red-brown colored NC solution (the inset in Fig. 1a) shows a molecule-like optical absorption nature with two distinct absorption peaks at 476 and 405 in the visible light region (Fig. 1a). The peak at 476 nm arises from the intraband (sp ← sp) transition, while the peak at 405 nm results from the combination of intraband (sp ← sp) and interband (d ← sp) transitions. The well-defined absorption peaks manifest a very high quality of raw NCs, which is evidenced by the electrospray ionization mass spectrometry (ESI-MS) spectrum (Fig. 1b). This spectrum reveals three distinct sets of main peaks at *m*/*z* 1934, 1439, and 1173, corresponding to $[Ag_{28}Au_1(DHLA)_{12}–2H]^{3-}$, $[Ag_{28}Au_1(DHLA)_{12}–3H]^{4-}$, and $[Ag_{28}Au_1(DHLA)_{12}–4H]^{5-}$, respectively. The experimental mass distribution of NCs closely aligns with the simulated distribution (Fig. S1†), affirming the successful preparation of $Ag_{28}Au_1$ NCs. Additionally, the transmission electron microscope (TEM) image shows that $Ag_{28}Au_1$ NCs are below 2 nm in size with an average size of ~1.7 nm (Fig. S2†), further corroborating the successful synthesis of ultrasmall NCs. Notably, the as-synthesized $Ag_{28}Au_1$ NCs show the typical AIE nature with a large Stokes shift exceeding 200 nm, as evidenced by their excitation and emission spectra (emitting red fluorescence (inset) with an emission peak at 645 nm (blue curve) upon excitation at 414 nm). Moreover, reducing the solution polarity by introducing an organic solvent (methanol) reinforces the aggregation state of the AIE-type $Ag_{28}Au_1$ NCs and constrains their nonradiative relaxation, leading to the enhancement of PL intensity (Fig. S3†). It was also found that although the Au-doped $Ag_{28}Au_1$ NCs have similar optical absorption to Ag_{29} NCs (Fig. S4†), they exhibit almost 4.7 times luminescence enhancement (Fig. 1c). The enhanced FL intensity of Ag_{29} NCs after a single Au atom doping can primarily be attributed to the enhanced structural stability and intramolecular interaction after Au atom doping, thereby inhibiting non-radiative transitions and ultimately leading to a stronger fluorescence response. This enhanced luminescence makes $Ag_{28}Au_1$ NCs the ideal antibacterial materials in terms of their efficient generation of photoinduced charge carriers, and this is why we chose gold–silver alloy NCs. Concurrently, the time-resolved PL profile of $Ag_{28}Au_1$ NCs contains two components (Fig. 1d): a short-lived PL lifetime of 0.61 μs (τ_1, derived from the interband transition (d ← sp) of the metal cores) and a

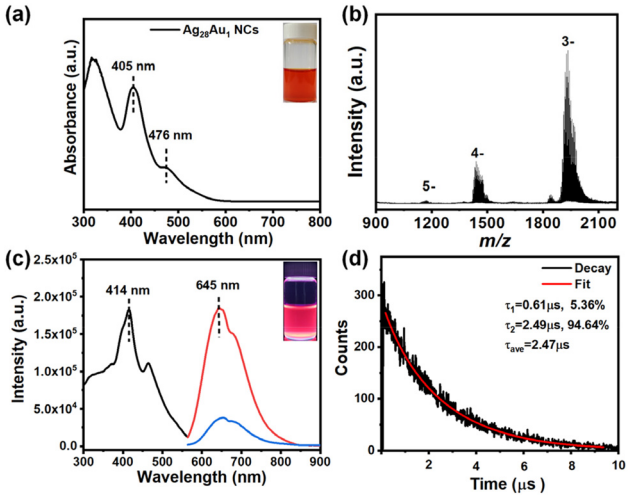

Fig. 1 (a) UV–visible absorption (inset: optical photo of $Ag_{28}Au_1$ NC solution under visible light illumination) and (b) ESI-MS spectrum of $Ag_{28}Au_1$ NCs. (c) Photoexcitation (black curve) and photoemission spectra (red curve) of $Ag_{28}Au_1$ NCs, and photoexcitation (green curve) and photoemission spectrum of Ag_{29} NCs (blue curve). (d) PL decay profile and the corresponding fit curve of the $Ag_{28}Au_1$ NCs. The inset shows the calculated PL lifetimes according to the fit curve (τ_{ave}: average PL lifetime).

long-lived PL lifetime of 2.49 μs (τ_2, caused by the ligand-to-metal or ligand-to-metal–metal charge transfer). The dominant contribution of τ_2 (94.64%) indicates that $Ag_{28}Au_1$ NCs possess long-lived photoluminescence (PL) lifetimes up to the μs-level (2.47 μs), surpassing the lifetimes of most AIE-free metal NCs (typically in the ps or ns range). Notably, the large Stokes shift, strong PL and long-lived PL lifetime are typical characteristics of AIE-type metal NCs, which are highly desirable for achieving highly efficient photodynamic antibacterial activity.

$Ag_{28}Au_1$ NCs@ZIF-8 was synthesized in the presence of AIE-type $Ag_{28}Au_1$ NC stock solution and ZIF-8 precursor. As shown, the obtained $Ag_{28}Au_1$ NCs@ZIF-8 display a regular rhombic dodecahedral structure with a diameter of around 600 nm (Fig. 2a), with ultrasmall black spot particles, each below 2 nm in size, uniformly spread throughout the ZIF-8 (Fig. 2b), indicating the successful encapsulation of AIE-type $Ag_{28}Au_1$ NCs into porous ZIF-8. Furthermore, the energy dispersive X-ray (EDX) elemental mapping (Fig. 2c) images provide visual evidence of good distribution of $Ag_{28}Au_1$ NCs in ZIF-8. Notably, the encapsulation of $Ag_{28}Au_1$ NCs did not change the size and crystal structure of ZIF-8, as evidenced by their similar sizes (Fig. S5†) and X-ray diffraction (XRD) patterns (Fig. 2d). In addition, Fourier-transform infrared (FTIR) analysis was performed to further determine the interaction between AIE-type $Ag_{28}Au_1$ NCs and ZIF-8. The FTIR spectrum of $Ag_{28}Au_1$ NCs@ZIF-8 shows similarity to that of ZIF-8, except for the emergence of a peak at 650 cm^{-1} corresponding to the Zn–O stretching vibration, confirming the interaction between COO^- in NCs and Zn^{2+} in ZIF-8 (Fig. S6†). Concurrently, the X-ray photoelectron spectra (XPS) reveal that the binding energy of Ag_{3d} and S_{2p} in $Ag_{28}Au_1$ NCs@ZIF-8 shows an increase of about 0.31 eV and 0.44 eV, respectively, compared to that of pristine $Ag_{28}Au_1$ NCs (Fig. 2e and Fig. S7†), suggesting a reduction in the electron density of the Ag and S elements in $Ag_{28}Au_1$ NCs@ZIF-8. Conversely, the binding energy of Zn_{2p} shows a negative shift of approximately 0.36 eV compared to that of pristine ZIF-8 (Fig. 2f), indicating an increase in the electron density of the Zn element in $Ag_{28}Au_1$ NCs@ZIF-8. Based on the above analysis, we may conclude that the AIE-type $Ag_{28}Au_1$ NCs were successfully confined into ZIF-8, and their interaction promotes charge transfer from the Ag and S elements in AIE-type $Ag_{28}Au_1$ NCs to the Zn element in ZIF-8, which contributes to improving the stability and promoting the separation of photoinduced charge carriers in AIE-type $Ag_{28}Au_1$ NCs.

3.2. Photodynamic antibacterial tests *in vitro*

After the successful preparation of $Ag_{28}Au_1$ NCs@ZIF-8, its photodynamic antibacterial activity was investigated by using representative Gram-negative (*E. coli*) and Gram-positive (*S. aureus*) bacteria. As shown in Fig. 3, the as-deigned $Ag_{28}Au_1$ NCs@ZIF-8 effectively killed over 97% of *E. coli* and 91% of *S. aureus* within 5 min (Fig. 3a and b) and over 99.8% of *E. coli* (2.7 orders of magnitude reduction in colony-forming unit (CFU; Fig. 3c)) and 99.2% of *S. aureus* (2.1 orders of magnitude reduction in CFU; Fig. 3d) within 20 min under visible-light illumination ($\lambda \geq 400$ nm) and O_2 bubbling. Additionally, $Ag_{28}Au_1$ NCs@ZIF-8 consistently exhibited superior antibacterial efficacy against Gram-negative bacteria compared to Gram-positive bacteria, owing to the heightened susceptibility of Gram-negative bacteria with their thinner cell walls rendering them more vulnerable to destruction by ROS. Conversely, pristine $Ag_{28}Au_1$ NCs, ZIF-8, and their blended sample ($Ag_{28}Au_1$ NCs + ZIF-8) did not exhibit similar photodynamic antibacterial activity under the same conditions (Fig. S8 and S9†). The enhanced antibacterial activity of $Ag_{28}Au_1$ NCs@ZIF-8 can be attributed to the encapsulation of $Ag_{28}Au_1$ NCs into ZIF-8, which improves the stability of $Ag_{28}Au_1$ NCs and facilitates the separation of photoinduced charge carriers, thereby enhancing the generation of destructive ROS for bacterial eradication.

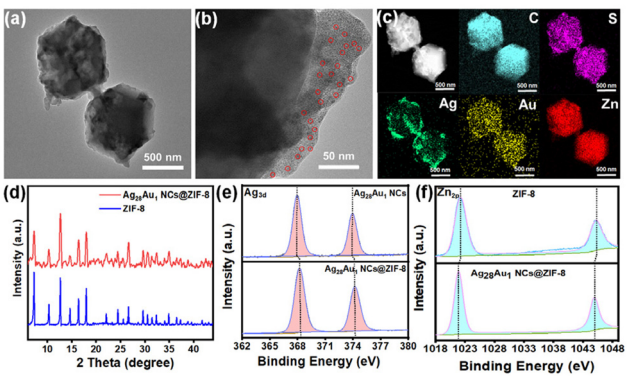

Fig. 2 TEM image (a) and the enlarged TEM image (b) of $Ag_{28}Au_1$ NCs@ZIF-8. (c) The EDX elemental mapping of C, S, Ag, Au and Zn of $Ag_{28}Au_1$ NCs@ZIF-8. (d) XRD patterns of $Ag_{28}Au_1$ NCs@ZIF-8 and ZIF-8. (e) High-resolution XPS of Ag_{3d} in $Ag_{28}Au_1$ NCs@ZIF-8 and $Ag_{28}Au_1$ NCs. (f) High-resolution XPS of Zn_{2p} in $Ag_{28}Au_1$ NCs@ZIF-8 and ZIF-8.

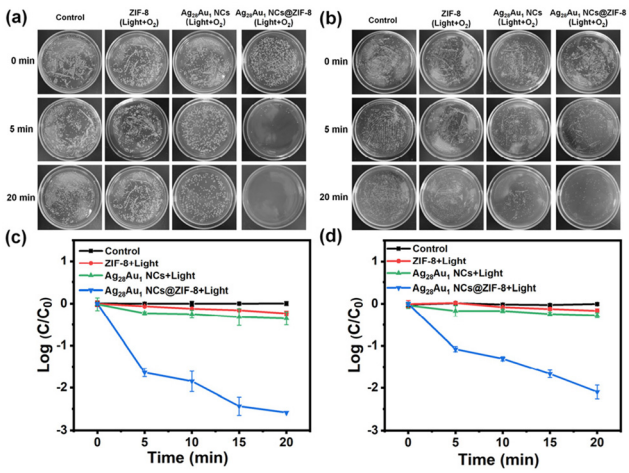

Fig. 3 Bacterial colony growth of (a) *E. coli* and (b) *S. aureus* in the presence of various samples under O_2 bubbling and visible-light illumination for 20 min, and treatment without any agent under dark conditions (control) for 20 min. Bactericidal activities of different samples against (c) *E. coli* and (d) *S. aureus*.

The mechanism will be discussed later. Moreover, the control experiment under light illumination and O_2 bubbling (light + O_2) indicates that light and O_2 have no significant effect on bacterial killing. Notably, the bacterial eradication efficacy of $Ag_{28}Au_1$ NCs@ZIF-8 was demonstrated by its ability to eliminate 94.1% of *E. coli* and 92.2% of *S. aureus* within 20 min under light illumination and exposure to air ($Ag_{28}Au_1$ NCs@ZIF-8 + light). Conversely, no significant bacterial killing was observed under dark conditions ($Ag_{28}Au_1$ NCs@ZIF-8), indicating the crucial roles of light illumination and O_2 (air) in the bacterial eradication process (Fig. S8 and S9†). These results suggest that the encapsulation of $Ag_{28}Au_1$ NCs into ZIF-8 achieves rapid bacterial eradication, making $Ag_{28}Au_1$ NCs@ZIF-8 a promising photodynamic antibacterial agent for the treatment of bacteria-infected wounds.

3.3. The antibacterial mechanism of $Ag_{28}Au_1$ NCs@ZIF-8

The investigation into the enhanced photodynamic antibacterial mechanism involved measuring the light absorption capability of pristine $Ag_{28}Au_1$ NCs, ZIF-8, and $Ag_{28}Au_1$ NCs@ZIF-8 because light absorption is a prerequisite for photodynamic bacterial eradication. The UV-visible diffuse reflection spectroscopy (DRS) results reveal that the pristine ZIF-8 sample has poor light harvesting ability in the visible light region due to its large energy gap (Eg) (Fig. 4a), which could explain its low photodynamic antibacterial activity under visible light illumination. Conversely, $Ag_{28}Au_1$ NCs@ZIF-8 exhibits characteristic peaks of $Ag_{28}Au_1$ NCs (Fig. 1a) and demonstrates excellent light harvesting capability in the visible-light region (400 to 780 nm), indicating that the optical absorption capability of $Ag_{28}Au_1$ NCs@ZIF-8 is mainly derived from $Ag_{28}Au_1$ NCs. Although the encapsulation of $Ag_{28}Au_1$ NCs into ZIF-8 had no significant effect on enhanced light absorption of $Ag_{28}Au_1$ NCs, it significantly promotes the separation of photoinduced charge carriers in $Ag_{28}Au_1$ NCs, which is another important factor in determining photodynamic antibacterial activity. As shown in Fig. 4b, an apparent quenching effect on the highly luminescent $Ag_{28}Au_1$ NCs was observed after the introduction of ZIF-8. Moreover, the photostability of $Ag_{28}Au_1$ NCs significantly improved when encapsulated into ZIF-8. Fig. S10† shows that the characteristic peaks of $Ag_{28}Au_1$ NCs gradually disappeared under light irradiation within 5 min, implying the destruction of the basic structure of $Ag_{28}Au_1$ NCs. This result suggests that the pristine $Ag_{28}Au_1$ NCs possess poor photostability, which is responsible for the low photodynamic antibacterial activity. Encouragingly, the encapsulation of $Ag_{28}Au_1$ NCs into ZIF-8 resulted in excellent stability against light irradiation for 210 min (Fig. 4c), showcasing the effectiveness of this encapsulation strategy in improving the photostability of metal NCs. These results imply that the encapsulation of $Ag_{28}Au_1$ NCs into ZIF-8 not only promotes the separation of photoinduced charge carriers in $Ag_{28}Au_1$ NCs but also improves the photostability of $Ag_{28}Au_1$ NCs.

The conduction band (CB) and valence band (VB) levels of $Ag_{28}Au_1$ NCs@ZIF-8 were measured as they are crucial in determining ROS generation, given that ROS (superoxide ($O_2^{\bullet-}$), hydrogen peroxide (H_2O_2), and hydroxyl radicals ($^{\bullet}OH$)) are the main active species for bacterial eradication. The energy gap (E_g) and the VB level of $Ag_{28}Au_1$ NCs@ZIF-8 were determined to be 1.81 eV and 1.73 eV (*vs.* normal hydrogen electrode (NHE)) according to the UV-visible DRS (Fig. S11†) and VB-XPS (Fig. S12†), respectively. Subsequently, the calculated CB level of $Ag_{28}Au_1$ NCs@ZIF-8 was found to be −0.08 eV (*vs.* NHE), indicating a thermodynamically favorable condition for the generation of $O_2^{\bullet-}$ and H_2O_2 *via* O_2 reduction, as it is more negative than the potentials for O_2 reduction ($O_2/O_2^{\bullet-}$, −0.046 V *vs.* NHE, and O_2/H_2O_2, 0.695 V *vs.* NHE) (Fig. 4d). Additionally, the VB level is higher than the potentials for H_2O and H_2O_2 oxidation (H_2O/O_2, 1.23 V *vs.* NHE, $H_2O_2/^{\bullet}OH$, 1.14 V *vs.* NHE), and it is sufficient to drive H_2O oxidation for O_2 generation and H_2O_2 oxidation for $^{\bullet}OH$ generation. To evaluate the production of ROS over various samples under light irradiation, the luminescent 2′,7′-dichlorofluorescein (DCF) was used as an indicator. The PL intensity of DCF treated with $Ag_{28}Au_1$ NCs@ZIF-8 was significantly higher than that of other groups (Fig. 4e), indicating the highest amount of ROS production. This can be attributed to the encapsulation of $Ag_{28}Au_1$ NCs into ZIF-8 which enhances their photostability and promotes the separation of photoinduced charge carriers. Consequently, the results of the ROS generation assay explain the highest photodynamic antibacterial efficiency of $Ag_{28}Au_1$ NCs@ZIF-8. Furthermore, the morphologies of bacteria before and after photodynamic bactericidal treatment were observed using a scanning electron microscope (SEM), revealing drastic changes in the morphologies of *S. aureus* (round) and *E. coli* (rod-shaped) from plump, smooth, and intact to collapsed, wrinkled, and cracked (Fig. 4f). These changes can be attributed to the destruction and oxidation of the bacterial cell membrane by photo-induced ROS, ultimately leading to their inactivation.

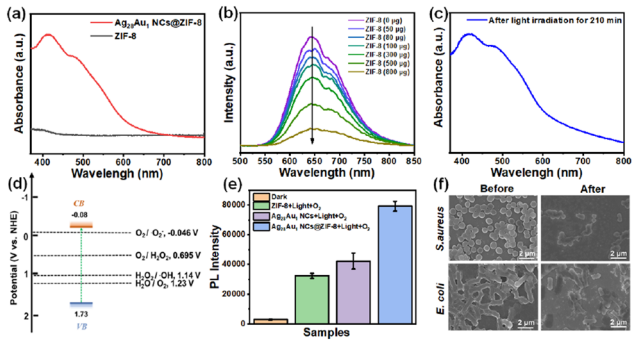

Fig. 4 (a) UV-visible DRS spectra of $Ag_{28}Au_1$ NCs@ZIF-8 and ZIF-8. (b) PL emission spectra of $Ag_{28}Au_1$ NC solution in the presence of different amounts of ZIF-8. (c) UV-visible DRS spectrum of $Ag_{28}Au_1$ NCs@ZIF-8 after light irradiation for 210 min. (d) The diagram of energy levels of $Ag_{28}Au_1$ NCs@ZIF-8. (e) The PL intensity of DCF treated with PBS under dark conditions (control group), and that with antibacterial agents under light irradiation and O_2 bubbling for 20 min. (f) SEM images of the bacteria before and after the photodynamic antibacterial test.

3.4. *In vivo* wound healing assessment

Based on the rapid bacterial eradication achieved by $Ag_{28}Au_1$ NCs@ZIF-8, the therapeutic ability of $Ag_{28}Au_1$ NCs@ZIF-8 (dispersed in carbomer, a commercially available hydrogel) was investigated using *S. aureus*-infected wounds as a model (Fig. 5a). Before that, the cytotoxicity of various antibacterial agents was assessed on HeLa cells, and the results demonstrated good viability of HeLa cells (89.8 ± 1.6%) after treatment with the hydrogel of $Ag_{28}Au_1$ NCs@ZIF-8 for 24 hours as depicted in Fig. S13.† This can be attributed to the natural biocompatibility of carbomer and the low toxicity of $Ag_{28}Au_1$ NCs@ZIF-8. The wound healing process was recorded using a digital camera, and the images obtained are presented in Fig. 5b. It was observed that all wound sizes began to decrease after 3 days of treatment (Fig. 5c). Notably, the wound size of mice treated with $Ag_{28}Au_1$ NCs@ZIF-8 was smaller than that in other groups on day 3, indicating efficient infection control attributed to the rapid bacterial eradication activity of $Ag_{28}Au_1$ NCs@ZIF-8. By day 7, the wound size of mice treated with $Ag_{28}Au_1$ NCs@ZIF-8 decreased to 6.3 ± 3.1 from 52.3 ± 1.7 mm^2 (Fig. 5d), with a wound healing rate of 88.0% (Fig. 5e). In contrast, the wound sizes of the control group and those treated with ZIF-8 and $Ag_{28}Au_1$ NCs were 17.0 ± 2.6, 11.8 ± 3.0, and 10.9 ± 1.5 mm^2, respectively, with wound healing rates of 72.8%, 81.8%, and 82.4%. After 11 days, only the wound treated with $Ag_{28}Au_1$ NCs@ZIF-8 was completely repaired and grew new epidermal tissue, while the wounds of the control group and those treated with ZIF-8 and $Ag_{28}Au_1$ NCs remained rough and irregular with 7.9%, 5.8%, and 3.8% of unhealed wound, respectively. Additionally, $Ag_{28}Au_1$ NCs@ZIF-8 showed similar wound size and healing rate to vancomycin (Van), a commercial antibacterial agent, suggesting the great potential of $Ag_{28}Au_1$ NCs@ZIF-8 in clinical application. These findings indicate that $Ag_{28}Au_1$ NCs@ZIF-8 significantly enhances the healing of bacteria-infected wounds by rapidly generating photodynamic ROS for bacterial eradication.

The effect of $Ag_{28}Au_1$ NCs@ZIF-8 on skin regeneration was assessed using hematoxylin and eosin (H&E) and Masson staining. The wounds treated with $Ag_{28}Au_1$ NCs@ZIF-8 displayed the best wound repair effect with respect to inflammatory cells, histological indicators of blood vessels, and the generation of epithelial tissue and collagen. Specifically, the wounds treated with $Ag_{28}Au_1$ NCs@ZIF-8 showed almost no inflammatory cells, while wounds without treatment or those treated with other antibacterial agents still presented some inflammatory cells (Fig. 6a, yellow arrows). This demonstrated that wounds treated with $Ag_{28}Au_1$ NCs@ZIF-8 could efficiently reduce the levels of inflammation, which could be attributed to their rapid photodynamic bacterial eradication activity. This conclusion is further supported by the expression levels of anti-inflammatory factors in wounds. As shown, the expression levels of interleukin-1β (IL-1β, Fig. 6b), tumor necrosis factor-α (TNF-α, Fig. 6c), and interleukin-6 (IL-6, Fig. 6d) in wounds treated with $Ag_{28}Au_1$ NCs@ZIF-8 were lower than those in other groups. Additionally, the distribution of blood vessels in wound tissue was assessed, as blood vessels play a crucial role in accelerating wound healing by transporting oxygen and nutrients. The wounds treated with $Ag_{28}Au_1$ NCs@ZIF-8 have a higher distribution of blood vessels compared to the other groups (red arrows), suggesting that $Ag_{28}Au_1$ NCs@ZIF-8 could promote the generation of new blood vessels in regenerated tissues. Furthermore, the new epithelial tissue in the wound treated with $Ag_{28}Au_1$ NCs@ZIF-8 is more uniform and structured compared with other groups (blue arrows), which is consistent with the observed wound repair results, manifesting the good tissue repair capacity of $Ag_{28}Au_1$ NCs@ZIF-8. Additionally, $Ag_{28}Au_1$ NCs@ZIF-8 showed similar therapeutic effects to Van, as evidenced by the similar H&E and Masson staining results in terms of the level of inflammation, the dis-

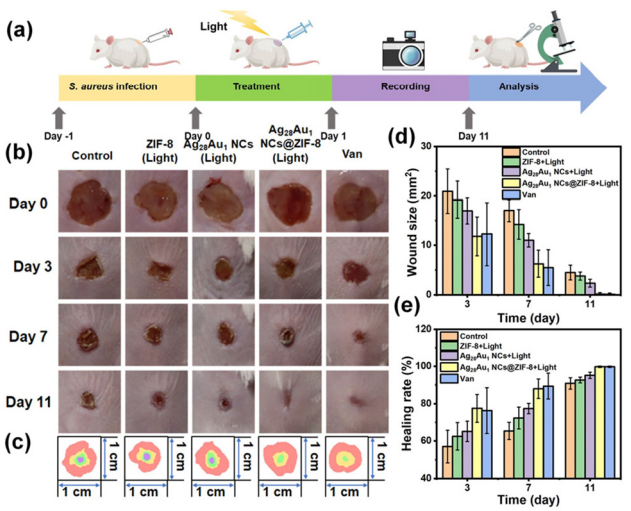

Fig. 5 (a) Schematic illumination of the antibacterial agents for wound healing *in vivo*. (b) Representative pictures of the incisional skin wounds treated with various antibacterial agents using carbomer as reference (control) at the specified time. (c) The simulation of wound areas in different groups over time. (d) Representative changes in wound size in different groups over time. (e) Representative changes of healing rate in different groups over time.

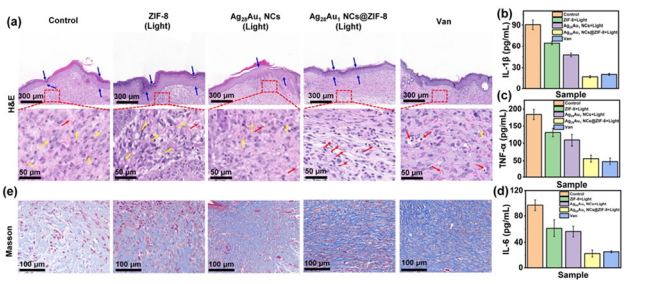

Fig. 6 (a) Representative H&E staining pictures of tissue slices collected from different groups on day 11 (yellow arrows point to the inflammatory cells, red arrows point to the blood vessels and blue arrows point to the epithelial tissue). The expression levels of IL-1β (b), TNF-α (c) and IL-6 (d) in blood collected from different groups on day 11. (e) Representative Masson staining pictures of tissue slices collected from different groups on day 11 (the blue area represents the collagen fiber).

tribution of blood vessels, and the generation of epithelial tissue and collagen, further supporting the potential of $Ag_{28}Au_1$ NCs@ZIF-8 for clinical applications.

The collagen contents (an important indicator to assess the generation stage from the inflammatory period to the recovery period) in the wound area were characterized by Masson staining. As shown in Fig. 6e and Fig. S14,† the collagen content (blue area) in the wound treated with $Ag_{28}Au_1$ NCs@ZIF-8 was higher compared to that in the other groups. Moreover, collagen in wounds treated with $Ag_{28}Au_1$ NCs@ZIF-8 exhibited orderly arranged and dense structures, while collagen in the other groups was in a degradation state, which might be due to the destruction by collagenase secreted by bacteria. Overall, the encapsulation of AIE-type $Ag_{28}Au_1$ NCs into ZIF-8 achieved rapid bacterial eradication, reduced the expression of inflammatory factors, and promoted the generation of new blood vessels, collagen, and epithelial tissue, thus demonstrating a favorable wound repair effect.

4. Conclusion

In summary, we have successfully developed an AIE-type metal NC-based photodynamic antibacterial agent for rapid bacterial eradication to facilitate wound healing under visible light irradiation by encapsulating AIE-type $Ag_{28}Au_1$ NCs into porous ZIF-8. It was found that the encapsulation strategy is beneficial to improving photostability and the separation of charge carriers in $Ag_{28}Au_1$ NCs, thereby facilitating the generation of destructive ROS for bacterial killing. As a result, the as-developed $Ag_{28}Au_1$ NCs@ZIF-8 demonstrated superior photodynamic antibacterial efficacy, killing 97.7% of *E. coli* and 91.6% of *S. aureus* within 5 min under visible light irradiation. Moreover, $Ag_{28}Au_1$ NCs@ZIF-8 showed good efficacy in the treatment of bacteria-infected wounds because of their rapid antibacterial action, antiinflammation, and ability to stimulate blood vessel and epithelial tissue growth. The strategy and design presented in this work may inspire the development of other metal NC-based photodynamic antibacterial agents for enhancing wound healing.

Ethics statement

All animal procedures were performed in accordance with the Guidelines for Care and Use of Laboratory Animals of Qingdao University of Science and Technology and approved by both the Animal Ethics Committee of Qingdao University of Science and Technology and the Animal Ethics Committee of Qingdao Zhong Hao Biological Engineering Co., Ltd (Qingdao, China).

Data availability

The data that support the findings of this study are available from the corresponding author (Haiguang Zhu) upon reasonable request.

Conflicts of interest

There are no conflicts to declare.

Acknowledgements

This work is supported by the National Natural Science Foundation of China (22071127, 22371153), the Taishan Scholar Foundation (tsqn201812074, China), and the Youth Innovation Team Development Program of Shandong Higher Education Institutions (2022KJ155).

References

1 S. R. Barman, S.-W. Chan, F.-C. Kao, H.-Y. Ho, I. Khan, A. Pal, C.-C. Huang and Z.-H. Lin, *Sci. Adv.*, 2023, **9**, eadc8758.
2 Z. Lu, S. Du, J. Li, M. Zhang, H. Nie, X. Zhou, F. Li, X. Wei, J. Wang, F. Liu, C. He, G. Yang and Z. Gu, *Adv. Mater.*, 2023, **35**, 2303388.
3 W. Zhou, Z. Duan, J. Zhao, R. Fu, C. Zhu and D. Fan, *Bioact. Mater.*, 2022, **17**, 1–17.
4 Y. Meng, L. Chen, Y. Chen, J. Shi, Z. Zhang, Y. Wang, F. Wu, X. Jiang, W. Yang, L. Zhang, C. Wang, X. Meng, Y. Wu and W. Bu, *Nat. Commun.*, 2022, **13**, 7353.
5 L. He, Y. Liu, P. Song, F. Feng, G. Li, Y. Ma, J. Cui, X. Ma, J. Shen and J. Zhang, *ACS Sustainable Chem. Eng.*, 2023, **11**, 11529–11540.
6 H. Chen, Y. Cheng, J. Tian, P. Yang, X. Zhang, Y. Chen, Y. Hu and J. Wu, *Sci. Adv.*, 2020, **6**, eaba4311.
7 Y. Hu, H. Zhou, J. Huang, T. Wang, H. Wang, D. Wu, C. Yu, G. Pan, L. Zhang, L. Zhang, D. Gou and J. Zhang, *ACS Sustainable Chem. Eng.*, 2023, **11**, 5122–5134.
8 J. Wang, Q. Meng, Y. Ma, Y. Yang, R. Zhang, S. Zhong, J. Wang, Y. Gao and X. Cui, *ACS Sustainable Chem. Eng.*, 2023, **11**, 18074–18088.
9 J. J. Kelly, B. E. Dalesandro, Z. Liu, M. D. Chordia, G. M. Ongwae and M. M. Pires, *Angew. Chem., Int. Ed.*, 2023, **63**, e202313870.
10 S. Kayama, K. Yahara, Y. Sugawara, S. Kawakami, K. Kondo, H. Zuo, S. Kutsuno, N. Kitamura, A. Hirabayashi, T. Kajihara, H. Kurosu, L. Yu, M. Suzuki, J. Hisatsune and M. Sugai, *Nat. Commun.*, 2023, **14**, 8046.
11 A. R. Brochado, A. Telzerow, J. Bobonis, M. Banzhaf, A. Mateus, J. Selkrig, E. Huth, S. Bassler, J. Zamarreño Beas, M. Zietek, N. Ng, S. Foerster, B. Ezraty, B. Py, F. Barras, M. M. Savitski, P. Bork, S. Göttig and A. Typas, *Nature*, 2018, **559**, 259–263.
12 L. Wang, X. Fan, M. Gonzalez Moreno, T. Tkhilaishvili, W. Du, X. Zhang, C. Nie, A. Trampuz and R. Haag, *Adv. Sci.*, 2022, **9**, 2105668.
13 B. Ran, L. Ran, Z. Wang, J. Liao, D. Li, K. Chen, W. Cai, J. Hou and X. Peng, *Chem. Rev.*, 2023, **123**, 12371–12430.

14 W. Li, C. Wang, Y. Yao, C. Wu, W. Luo and Z. Zou, *Trends Chem.*, 2020, **2**, 1126–1140.
15 N. Yang, C. Cao, X. Lv, T. Zhang, J. Shao, X. Song, W. Wang, P. Chen, W. Huang and X. Dong, *BMEMat*, 2023, **1**, e12005.
16 B. Ran, Z. Wang, W. Cai, L. Ran, W. Xia, W. Liu and X. Peng, *J. Am. Chem. Soc.*, 2021, **143**, 17891–17909.
17 S. Wang, W.-Y. Wu, J. C. C. Yeo, X. Y. D. Soo, W. Thitsartarn, S. Liu, B. H. Tan, A. Suwardi, Z. Li, Q. Zhu and X. J. Loh, *BMEMat*, 2023, **1**, e12021.
18 Y. Genji Srinivasulu, Q. Yao, N. Goswami and J. Xie, *Mater. Horiz.*, 2020, **7**, 2596–2618.
19 M. A. Abbas, P. V. Kamat and J. H. Bang, *ACS Energy Lett.*, 2018, **3**, 840–854.
20 B. Weng, K.-Q. Lu, Z. Tang, H. M. Chen and Y.-J. Xu, *Nat. Commun.*, 2018, **9**, 1543.
21 H. Wang, X. Liu, W. Yang, G. Mao, Z. Meng, Z. Wu and H.-L. Jiang, *J. Am. Chem. Soc.*, 2022, **144**, 22008–22017.
22 H. Shan, J. Shi, T. Chen, Y. Cao, Q. Yao, H. An, Z. Yang, Z. Wu, Z. Jiang and J. Xie, *ACS Nano*, 2023, **17**, 2368–2377.
23 F. Hu, R. L. He, Z. J. Guan, C. Y. Liu and Q. M. Wang, *Angew. Chem., Int. Ed.*, 2023, **62**, e202304134.
24 S.-S. Zhang, S. Havenridge, C. Zhang, Z. Wang, L. Feng, Z.-Y. Gao, C. M. Aikens, C.-H. Tung and D. Sun, *J. Am. Chem. Soc.*, 2022, **144**, 18305–18314.
25 Z. Xie, P. Sun, Z. Wang, H. Li, L. Yu, D. Sun, M. Chen, Y. Bi, X. Xin and J. Hao, *Angew. Chem., Int. Ed.*, 2020, **59**, 9922–9927.
26 Z. Yin, Z. Wang, X. Dai, N. Liu, S. Wang, G. Li, F. Du and X. Yuan, *ACS Sustainable Chem. Eng.*, 2020, **8**, 15336–15343.
27 K. Zheng and J. Xie, *ACS Nano*, 2020, **14**, 11533–11541.
28 D. Liu, W. Du, S. Chen, X. Kang, A. Chen, Y. Zhen, S. Jin, D. Hu, S. Wang and M. Zhu, *Nat. Commun.*, 2021, **12**, 778.
29 C. Yao, C. Q. Xu, I. H. Park, M. Zhao, Z. Zhu, J. Li, X. Hai, H. Fang, Y. Zhang, G. Macam, J. Teng, L. Li, Q. H. Xu, F. C. Chuang, J. Lu, C. Su, J. Li and J. Lu, *Angew. Chem., Int. Ed.*, 2020, **59**, 8270–8276.
30 M. Sugiuchi, J. Maeba, N. Okubo, M. Iwamura, K. Nozaki and K. Konishi, *J. Am. Chem. Soc.*, 2017, **139**, 17731–17734.
31 X. H. Wu, P. Luo, Z. Wei, Y. Y. Li, R. W. Huang, X. Y. Dong, K. Li, S. Q. Zang and B. Z. Tang, *Adv. Sci.*, 2018, **6**, 1801304.
32 Y. Yu, Z. Luo, D. M. Chevrier, D. T. Leong, P. Zhang, D.-E. Jiang and J. Xie, *J. Am. Chem. Soc.*, 2014, **136**, 1246–1249.
33 Y. E. Shi, J. Ma, A. Feng, Z. Wang and A. L. Rogach, *Aggregate*, 2021, **2**, e112.
34 S. Qian, Z. Wang, Z. Zuo, X. Wang, Q. Wang and X. Yuan, *Coord. Chem. Rev.*, 2022, **451**, 214268.
35 Y. Wang, Z. Zuo, Z. Wang, Y. Wu, J. Linghu, Y. Liu, H. Zhu, X. Dou, T. Feng and X. Yuan, *Chem. Eng. J.*, 2024, **492**, 152216.
36 Y. Duan, J. Luo, S. Zhou, X. Mao, M. W. Shah, F. Wang, Z. Chen and C. Wang, *Appl. Catal., B*, 2018, **234**, 206–212.
37 K. Liu, L. Wang, S. Li, H. Liu, D. Zhang, M. Jiang, W. Chen, F. Jiao, X. Zhang and W. Hu, *Adv. Funct. Mater.*, 2023, **33**, 2306871.
38 M. Wang, L. Nian, Y. Cheng, B. Yuan, S. Cheng and C. Cao, *Chem. Eng. J.*, 2021, **426**, 130832.
39 H. Lee, W. S. Chi, M. J. Lee, K. Zhang, F. Edhaim, K. Mizrahi Rodriguez, S. J. A. DeWitt and Z. P. Smith, *Adv. Funct. Mater.*, 2022, **32**, 2207775.
40 Z. Liu, Y. Yi, S. Wang, H. Dou, Y. Fan, L. Tian, J. Zhao and L. Ren, *ACS Nano*, 2022, **16**, 16549–16562.